Vol. 03, Iss. 1 (2025) 40-51, DOI: 10.61552/JME.2025.01.002

Journal of Materials and Engineering

www.jme.aspur.rs

Research article

Computational Analysis of Transient Solidification Kinetics in Aluminum-Based Multicomponent Alloys for Graphical LHTES Modelling

Ivaldo L. Ferreira[a,*], Natália Cristina A. Costa[a], Gueber Elias M. Santos Júnior[a], Fabrícia S. Gonzaga[a], Antonio Luciano S. Moreira[a]

[a]*Federal University of Pará, Augusto Corrêa Avenue 1, 66075-110, Belém, PA, Brazil.*

Keywords:

Latent heat thermal energy storage
Medium-temperature PCM
Multicomponent PCM
Thermal reservoir
Graphical-aided TES design

* Corresponding author:

Ivaldo Leao Ferreira
E-mail: ileao@ufpa.br

Received: 2 April 2024
Revised: 10 May 2024
Accepted: 16 June 2024

A B S T R A C T

Latent heat thermal energy storage (LHTES) is applied to heating, ventilation and air-conditioning (HVAC) systems. Thus, it is essential to use renewable energy sources such as solar, wind, sea and geothermal to ensure the reliability and availability of generated power in the consumer grid. PCMs are employed extensively and available as paraffin waxes, non-paraffinic organics, hydrated salts, pure metals and alloys. The numerical simulation of thermal energy storage (TES) reservoirs depends on the thermophysical and phase transformation properties to predict the behaviour of latent heat release. The phase transformation process is numerically non-trivial since it adds non-linear behaviour to the set of transport equations. This work develops a numerical model for the transient solidification of multicomponent alloys for medium-temperature PCM to elaborate a graphical solution for melting/solidifying PCM as auxiliary tools in the design of thermal reservoirs. The theoretical solution proposed for the microsegregation parameter β_i is based on the phase nucleation/growth radius, which is dependent on the thermal field tensor Γ in substitution of SDAS/2. The selection criterion of the alloys is based on the availability of thermophysical properties and phase diagrams. This is the first step in obtaining a data set for the AI designing-aid tool for LHTES reservoirs.

1. INTRODUCTION

The determination of melting and solidification kinetics of multicomponent alloy systems demands a coupling between thermal fields in the microscopic and macroscopic scales by binding the transport equations in both scales with the corresponding phase transitions. Among the methods available for solving the so-called Stefan problem can be mentioned analytical, semi-analytical and numerical methods. A comprehensive review of the

literature can be found in [1-8]. In the present scenario of Global Warming due to the high emission of greenhouse gases (GHG) by human activities [9], getting the most out of renewable sources concerning their availability and reliability to minimise the mismatch between supply and demand is imperative [10]. The abovementioned issue is addressed in terms of the latent heat thermal energy storage (LHTES). The thermal energy storage (TES) has since long been applied to heating, ventilation and air-conditioning (HVAC) systems to take advantage of lower electric tariffs [11,12] and also in many branches of industry [13]. The thermal storage reservoirs use a phase-change material (PCM) to store energy in the form of latent heat, e.g., by absorbing a high amount of energy during melting and releasing it during solidification. According to the type, PCM can be classified as organic (paraffin and fatty acids), inorganic (salt hydrates) and eutectic materials (organic and inorganic), relating their melting temperature (low, medium and high) to the latent heat of fusion. LHTES stores 5-14 times more heat than sensible heat thermal energy storage (SHTES) [14-18]. Recently, Maleki et al. [19] have investigated a combination of photovoltaic cells and thermoelectric generator (TEG)/dual-PCM to prevent it from overheating by improving its electrical efficiency. The maximum theoretical efficiency of thermal electric generator is 33% for high temperature of $T_H = 1400$K and $T_C = 300$K and $\Delta T = 1100$K, and the second most efficient range is 23.9% at $T_H = 1100$K and $T_C = 300$K, for $\Delta T = 800$K and the third is 17.1% at $T_H = 860$K and $T_C = 300$K, for $\Delta T = 560$K [20]. Solar thermal power plants use solar radiation to produce electricity and the generation worldwide was about 10GWe by 2021. Concerning the solar thermal power plant, it consists of two basic components: the solar field and the power block. There are four main concentrating solar technologies commercially available: linear Fresnel collector, parabolic trough collector, central receiver systems and parabolic dish. The power block can be classified according to the thermodynamic cycle, solar field and heat transfer fluid applied. The steam Rankine cycle is the most employed and commercially available configuration for the power block [21]. Due to the discontinuous nature of solar radiation, an intermediate medium is applied to transfer the thermal energy to the working fluid, the thermal energy storage. The strategy applied to TES can minimise the parasitic consumption of the plant and increase its overall efficiency as reported in [22,23].

In this paper, a numerical model previously applied to the study of solidification kinetics, solute segregation [5,24,25], microporosity formation [26,27] and the evaluation of thermophysical properties [28] of multicomponent alloys will be used to predict the kinetics of solidification of a medium-temperature PCM and to elaborate graphical solution of the thermal variables of solidification for a wide range of Biot and Fourier numbers.

2. MATHEMATICAL FORMULATION AND DIMENSIONLESS ANALYSIS

In heat conduction with phase change, the liquid-to-solid transformation can be described by a set of dimensionless numbers, i.e., *Biot* which is the ratio between convective and conductive thermal resistance, *Fo* is Fourier number defined as the heat diffusion capacity of the material with respect to the space and time scales, *Ste* is Stefan number defined as the ratio of sensible and latent heat, *Prandtl* is the ratio of momentum diffusivity and thermal diffusivity, *Re* is Reynolds number and corresponds to the ratio of inertial and viscous forces, and *Sc* is Schmidt number defined as the ratio of momentum diffusivity and mass diffusivity in assemblance of *Prandtl* number.

The dimensionless parameters and numbers applied for the solidification of PCM are the following:

$$z^* = \frac{z}{Z_b} \tag{1}$$

$$u^* = \frac{u}{u_\infty} \tag{2}$$

$$t^* = \frac{u_\infty}{Z_b}\, t \tag{3}$$

$$\Delta T = T_{(F,L,EUT)} \tag{4}$$

$$T^* = \frac{T - T_S}{\Delta T} \; or \; T^* = \frac{T}{\Delta T} \tag{5}$$

$$Pr = \frac{\nu}{\alpha} \tag{6}$$

$$Sc = \frac{\nu}{D} \quad (7)$$

$$Re = \frac{\rho\, u\, Z_b}{\mu} \quad (8)$$

$$Fo = \frac{\alpha\, t}{Z_b^2} \quad (9)$$

$$Ste = \frac{C_{PL}\, T_{(F,L,EUT)}}{\Delta H} \quad (10)$$

2.1 Numerical modeling

The numerical model adapted to this work for the simulation of the solidification process of pure metals and eutectic alloys is the same proposed by Swaminathan et al. [5], modified and applied to problems of inverse macrosegregation of multicomponent systems [24,25] and microporosity formation [26-28].

The numerical model modified by Ferreira et al. [24-28] encompasses the following characteristics:

1. It can deal with the coupling of temperature and composition fields and multiple reactions during solidification of multicomponent alloys, such as primary phase transformation, phase precipitations, eutectic and peritectic transformations;
2. It considers the effect of the difference in specific mass between the liquid and other primary and secondary phases during the solidification in the form of a shrinkage-induced flow;
3. A temperature rescaling is used to deal with the solidification of pure eutectic materials.

2.2 Model Assumptions

The numerical model for unsteady solidification of pure metals/compounds and multicomponent alloys is based on the following assumptions:

1. The domain is one-dimensional and finite, defined by $0 \le Z \le Z_b$ as shown in Fig. 1, in which the boundary conditions at $Z = 0$ are of third kind and at $Z = Z_b$ no heat and mass fluxes are allowed;
2. The phase change material (PCM) to be solidified is taken to be a pure metal or a multicomponent alloy;
3. The solid phase is stationary, i.e., once formed it has a velocity equal to zero;
4. In the case of a eutectic composition alloy, due to the relatively fast nature of heat and mass transport in an average microscopic element, the temperature T, the concentration C_{Li}, the specific mass ρ_L and the liquid velocity u_L are considered constant;
5. In a general case, in the phase diagram, the angular coefficient of the liquidus isotherm m_{Li} and the partition coefficient k_{0i} are taken to be constant, e.g., the mean integral value;
6. In a general case, equilibrium conditions at the solid/liquid interface are assumed, i.e., either $C_{Li} = 0$ for pure metal or $C_{Li} = C_{LEUTi}$, for eutectic reactions.

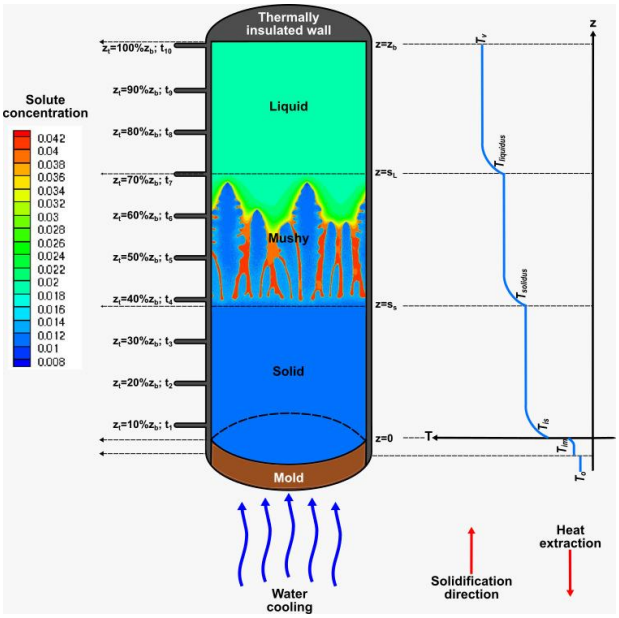

Fig. 1. Schematic representation of transient upward solidification cooled from the bottom.

$$T = T_F - \sum_{i=1}^{n} \frac{\partial T_L}{\partial C_{Li}} C_{L,i} = T_F - \sum_{i=1}^{n} m_{L,i}\, C_{L,i} \quad (11)$$

and,

$$C_S^* = k_0 C_L \quad (12)$$

where, T is the equilibrium temperature, C_i is the solute i concentration and T_F is the solvent melting temperature.

$$C_S^* \quad (13)$$

is the concentration of the solid at the interface, and the sub-indices S and L are relative to the solid and liquid phases.

2.3 Governing equations

The governing equations for the unsteady solidification of multicomponent alloys for general purpose must consider mass, energy and chemical species for general application,

- Mass

$$\frac{\partial \rho}{\partial t} + \nabla \cdot (\rho_L u) = 0 \quad (14)$$

- Energy

$$\frac{\partial \rho C_P T}{\partial t} + \nabla \cdot (\rho_L C_{PL} u T) = \nabla \cdot (k \nabla T) - \rho_S \, \Delta H \, \frac{\partial g}{\partial t} \quad (15)$$

- Chemical species

$$\frac{\partial \rho C_i}{\partial t} + \nabla \cdot (\rho_L u C_{Li}) = \nabla \cdot (D_i \, \nabla C_i) \quad (16)$$

The velocity field in the liquid can be updated by the value of the liquid volume fraction, g_l as $u = g_l u_l$.

- Boundary and initial conditions:

$$\text{At } z = 0,$$
$$u = 0, -k\frac{\partial T}{\partial z} = h_g(T|_{z=0} - T_\infty) \text{ and } \left.\frac{\partial C_i}{\partial z}\right|_{z=0} = 0 \quad (17)$$

$$\text{At } z = Z_b,$$
$$u \to u_\infty, \left.\frac{\partial T}{\partial z}\right|_{z=Z_b} = 0 \text{ and } \left.\frac{\partial C_i}{\partial z}\right|_{z=Z_b} = 0 \quad (18)$$

$$\text{At } t = 0, \text{ and } 0 \le Z \le Z_b,$$

$$u = 0, T(z) = -az^2 + bz + c, \text{ and } C_i = C_{0i} \quad (19)$$

2.4 Solution scheme

A finite volume method is applied for the solution of set of PDEs as previously proposed by Swaminathan and Voller [5], modified by Ferreira et al. [24,25,28] for parabolic initial temperature profile. It is worth mentioning that a rescale of temperature in terms of the solutes composition in the liquid phase is necessary for the coupling between temperature and concentration fields [5,24,29,30], i.e., for any temperature T, $T^* = T - T_F - \sum_{i=1}^{n} \frac{\partial T_L}{\partial C_{Li}} C_{L,i} = T - T_F - \sum_{i=1}^{n} m_{L,i} \, C_{L,i}$. For instance, to rescale liquidus temperature, $T_L^* = T_L - T_F - \sum_{i=1}^{n} \frac{\partial T_L}{\partial C_{Li}} C_{L,i} = 0$. The microscale model adopted in this work is that proposed by Brody-Flemings, modified by Clyne and Kurz [31] and associated later with the concentration density field [ρC] by Swaminathan and Voller [5] as the following,

$$[C_{L,i}]_P = \frac{[\rho C_{L,i}] - [\rho C_{L,i}]_P^{old} + [\rho_{L,i} \, g_P^{old} + \beta_i \, \rho_{S,i}(1 - g_P^{old}) k_{0,i}][C_{L,i}]_P^{old}}{\rho_{L,i} \, g_P^{old} + \beta_i \, \rho_{S,i}(1 - g_P^{old}) k_{0,i} + (1 - \beta_i) \, \rho_{S,i} \, k_{0,i}(g_P^{old} - g_P^{n+1})} \quad (20)$$

where the parameter β_i is the solute redistribution parameter, defined such that $0 \le \beta_i \le 1$. Making $\beta_i = 1$ gives the Lever Rule, and assuming $\beta_i = 0$ gives the Scheil equation for limiting cases. For $0 < \beta_i < 1$, it is the so-called finite diffusion. A detailed description of the calculation of the parameter β_i associated with solidification kinetics can be found in [29,30]. One possible solution for the back-diffusion parameter β_i is proposed by Swaminathan and Voller [5], as a function of compound Fourier number α_i, function γ_i and solid fraction $f\left(\frac{df}{d\tau}\right)$,

$$\beta_i = \frac{\alpha_i \, \gamma_i}{\alpha_i + \gamma_i \, f\left(\frac{df}{d\tau}\right)} \quad (21)$$

In the case of parabolic growth Eq. (21) can be expressed as,

$$\beta_i = \frac{2\alpha_i \, \gamma_i}{2\alpha_i + \gamma_i} \quad (22)$$

in which γ_i is a function of SDAS envelope compound Fourier α_i and partition coefficient k_i and parameter A [29],

$$\gamma_i = \frac{A \, \alpha_i \, k_i}{A \, \alpha_i \, k_i + 1} \quad (23)$$

and α_i is given by,

$$\alpha_i = \frac{4 \, D_i \, t_f}{SDAS^2} \quad (24)$$

where τ is the dimensionless time, f is the solid fraction, t_f is the solidification time for a Representative Elementary Volume [29], D_i is the diffusion coefficient of solute i and $SDAS$ is the secondary arm spacing in equilibrium [30] and non-equilibrium nucleation [32,33]. According to the authors $SDAS$ can be calculated in terms of Gibbs-Thomson coefficient [34] given by,

$$SDAS = 5.5 \, (M \cdot t_{SL})^{\frac{1}{3}} \quad (25)$$

and,

$$M = \frac{-\Gamma \sum_{j=1}^{n} w_j \beta_j}{\sum_{j=1}^{n} m_j \left(1 - \frac{k_j}{k_j + (1-k_j)\, exp\left(\frac{-\nu\, \delta_j}{D_j}\right)}\right) \left(c_{f,j} - c_{0,j}\right) / D_j} ln \left[\frac{\sum_{j=1}^{n} m_j \left(1 - \frac{k_j}{k_j + (1-k_j)\, exp\left(\frac{-\nu\, \delta_j}{D_j}\right)}\right) c_{f,j} / D_j}{\sum_{j=1}^{n} m_j \left(1 - \frac{k_j}{k_j + (1-k_j)\, exp\left(\frac{-\nu\, \delta_j}{D_j}\right)}\right) c_{0,j} / D_j} \right] \quad (26)$$

and the Gibbs-Thomson coefficient Γ is calculated from Gibbs-Thomson-Ferreira equation (GTF) [34] as dependent on the total superficial energy ∇E the thermal field gradient ∇T according to Eq. (27)

$$\Gamma = \mathrm{A} \cdot \nabla \mathrm{T} = \mathrm{A} \cdot \nabla \left[\frac{\partial T}{\partial E}\, E\right] = \mathrm{A} \cdot \left[\nabla \left(\frac{\partial T}{\partial E}\right) E + \frac{\partial T}{\partial E} \nabla E\right] \quad (27)$$

where, the thermal field gradient, $\nabla \left[\frac{\partial T}{\partial E}\, E\right] = \nabla \mathrm{T}$ can be referred to as the thermal field tensor Γ, in which the Gibbs-Thomson-Ferreira coefficient is expressed as $\Gamma = \mathrm{A} \cdot \nabla \left[\frac{\partial T}{\partial E}\, E\right] = \mathrm{A} \cdot \nabla \mathrm{T}$ and the identity $\mathrm{A} \cdot \nabla \left[\frac{\partial T}{\partial E}\, E\right] = \mathrm{A} \cdot \nabla \mathrm{T}$ is true.

It is well known that dependence of transformation isotherms on the melting temperature, chemical species, pressure, work, and other system variables can be calculated by taking account a new general physical entity named thermal field T which is defined by the thermodynamics first law, $Q - W = \sum_{i=1}^{n} E_i$, which affects the transformation temperature [34], redefining the Gibbs–Thomson scalar coefficient Γ as a novel tensor physical entity Γ,

$$\mathrm{T} = \frac{\partial T}{\partial E}\, E = T_F - \sum_{j=1}^{n} \frac{\partial T}{\partial n_i} n_i + \frac{\partial T}{\partial \boldsymbol{\sigma}} \sigma + \frac{\partial T}{\partial w} w + \frac{\partial T}{\partial \Sigma_{other}} \Sigma_{other} \quad (28)$$

in which $\sigma = \tau - p\, \mathrm{I}$, T_F is any transformation temperature, n_i is the number of moles of species i, w is the work, and Σ_{other} represents other forms of energy.

3. RESULTS AND DISCUSSION

An accurate description of transient solidification kinetics of multicomponent alloys for wide space and time scales requires the determination of both the thermal resistances evolution for the evolving solid phase, thermophysical and phase transformation properties. For latent heat thermal energy storage (LHTES) application for pure materials, approaches like in De London and Seban [35]. For heat release under a temperature range, kinetic can change the amount of heat release for the same alloy under different cooling conditions [5,24,29,30,32]. A total of 200h were spent in simulation to pose the thermal parameters and solidification variables in a suitable form to represent the evolution of dimensionless solidification. For instance, in the case of dimensionless surface temperature θ_i^*, two different sets of results are obtained by simply neglecting the shrinkage-induced flow [5,6]. The selection of the Al-6Cu-1Si and Al-6Cu-3Si (all in wt %) alloys to be analysed was based on the following criteria: The availability of both thermophysical and phase-transformation properties [26,27] provided in Table 1; A medium-temperature PCM [14] to permit being applied as LHTES for commercially available thermoelectric generators - TEG of intermediate performance [19] as well as for steam Rankine combined cycles [21]. Primary and secondary reactions such as precipitation of Si, LIQUID, FCC_A1, AL2CU and SILICON phases are considered through Thermo-Calc Application Programming Interface v.5 (TCAPI5) and Thermotech Thermal Aluminium Database - v.7. The code is written in Microsoft C++. The transport equations are solved by finite volume method (FVM) and the code is written for Intel (R) Fortran Intel (R) 64 Compiler Classic for applications running on Intel (R) 64, Version 2021.9.0 Build 20230302_000000. In unsteady solidification in cooled moulds, $Biot^{-1} = \frac{k_s}{h_G\, L}$ depends on the global heat transfer coefficient h_G, which is normally time-dependent, which can be expressed in the $h_G = a\, t^{-b}$ form, where a and b are constants [24,25]. In this case, there are two possible approaches for the application of graphical solution: In the first approach, a mean integral of $\overline{Biot}^{-1} = \frac{1}{t_{max}} \int_0^{t_{max}} Biot^{-1}(t) dt$ is calculated and used to determine the mean kinetics of heat release. In the second case, discrete values of $Biot^{-1}$ are determined as a function of time for each h_G to correct the kinetic. For instance, by considering $h_G = 6000\, t^{-0.12}$ [W m^{-2} K^{-1}], $L = 1$ [m] and $k_S = 180$ [W m^{-1} K^{-1}], as shown in Fig. 2.

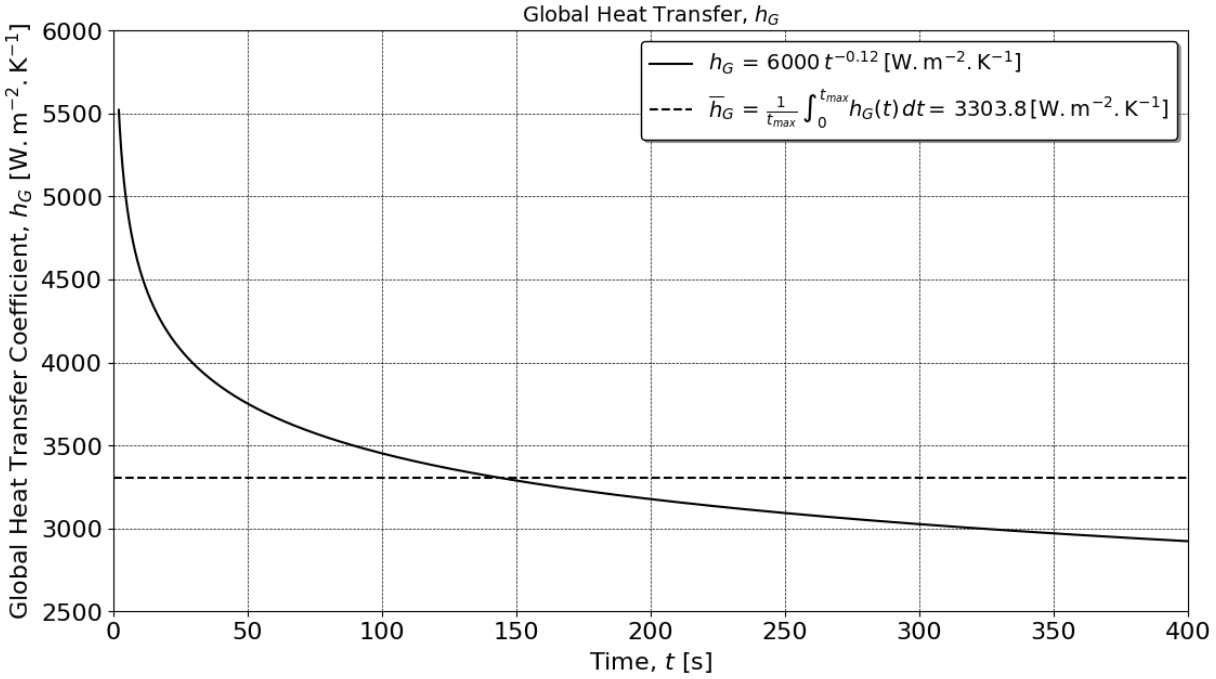

(a)

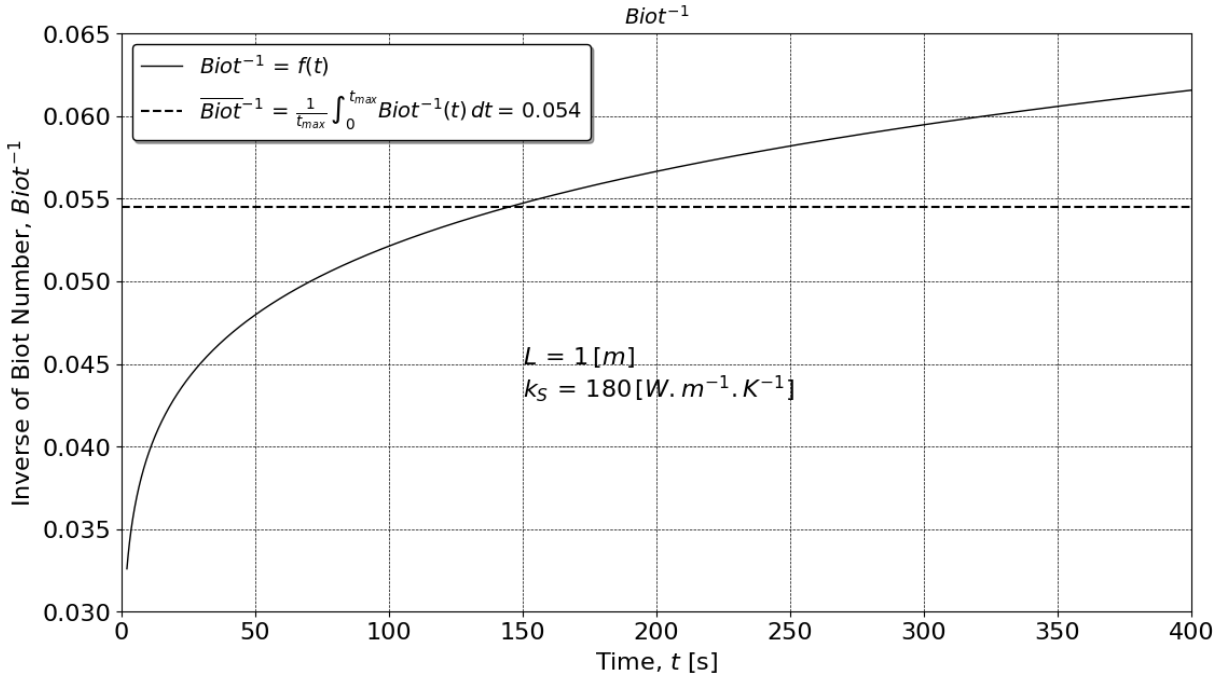

(b)

Fig. 2. Time dependence on, (a) global transient heat transfer coefficient, h_G; and (b) inverse of $Biot, Biot^{-1}$.

In Figure 3A, the SDAS calculations are carried out for the Al-3wt%Cu-9wt%Si alloy and plotted against the experimental data found in [30] as a necessary step for the evaluation of equations (22)-(24) related to the microsegregation parameter β_i for the Cu and Si solutes, a necessary procedure for correctly calculating the latent heat release in the mushy zone, as shown in Fig. 3B.

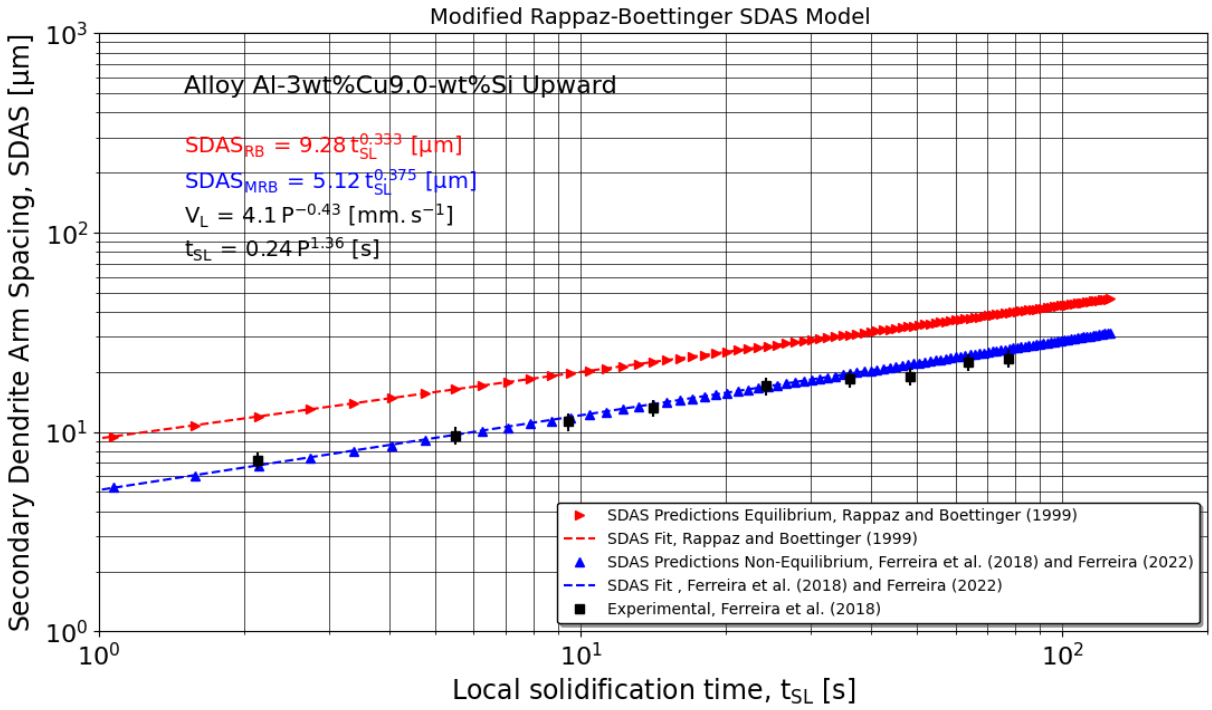

(a)

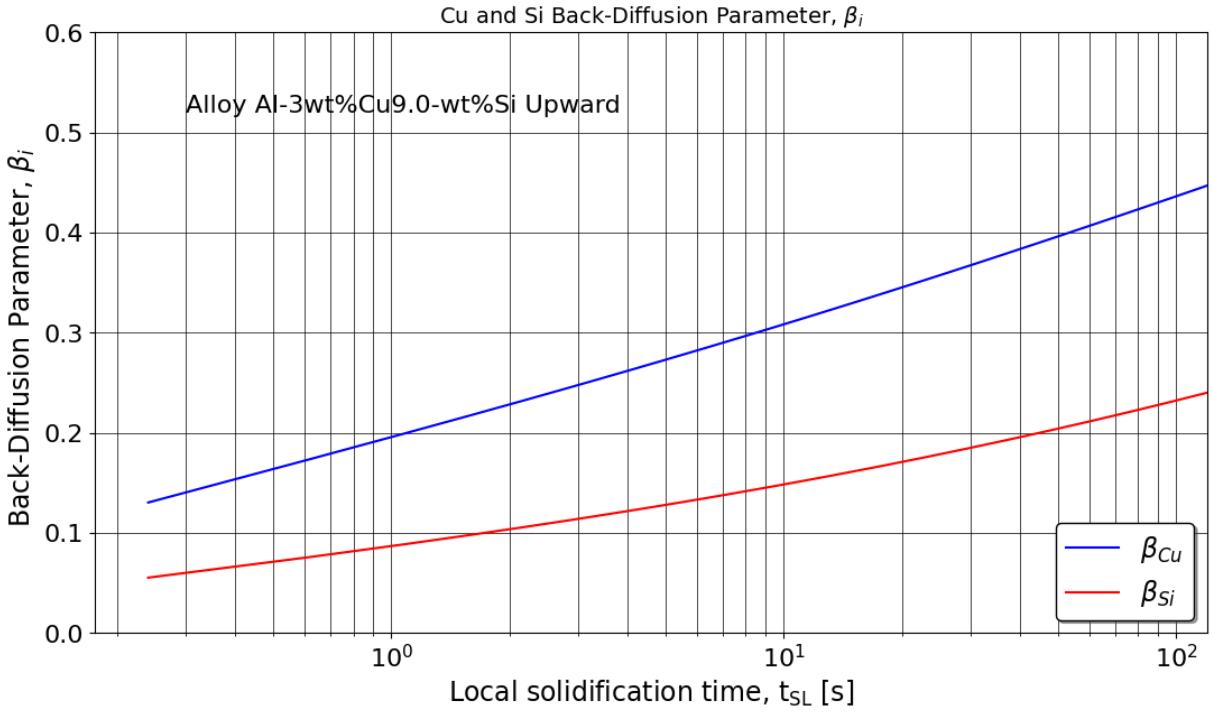

(b)

Fig. 3. Application of the modified Rappaz and Boettinger SDAS model to (A) determine secondary arm spacing, and (B) calculate local back-diffusion parameters.

In Figure 4, the dimensionless surface temperature $\frac{\theta(0,t)}{\theta_i}$ is plotted against Fourier number Fo of the liquid for a set of $Biot^{-1}$ curves for the investigated alloys. The simulation of surface cooling curves assume $dt = 5\,x\,10^{-4}\,s$ for $0.2 \leq Biot^{-1} \leq 2$, and $dt = 10^{-4}\,s$ for $0.005 \leq Biot^{-1} \leq 0.1$. The magnitude of time scale variation is about 10^6 s. The problem associated to the scales of space and time in the solution of PDE is a well-known problem [7]. In this paper, the simulation stopped as the eutectic isotherm reaches $S_{Eut} = L$ for application in

LHTES reservoirs. The effect of solidification range is noticed since it acts as a resistance to the evolution of the liquidus and eutectic isotherms, causing a faster solidification in the case of Al-6Cu-3Si (in wt%) alloy, as observed in Fig. 4 and Fig. 5. The dimensionless technique applied for the surface temperature profiles, despite having similar shapes due to different thermophysical properties. Thus, a new proposition for dimensionless temperature as a function of $Biot^{-1}$ must be derived. Nevertheless, within the same alloy it is valid for a wide range of space L, time t and $Biot$ scales.

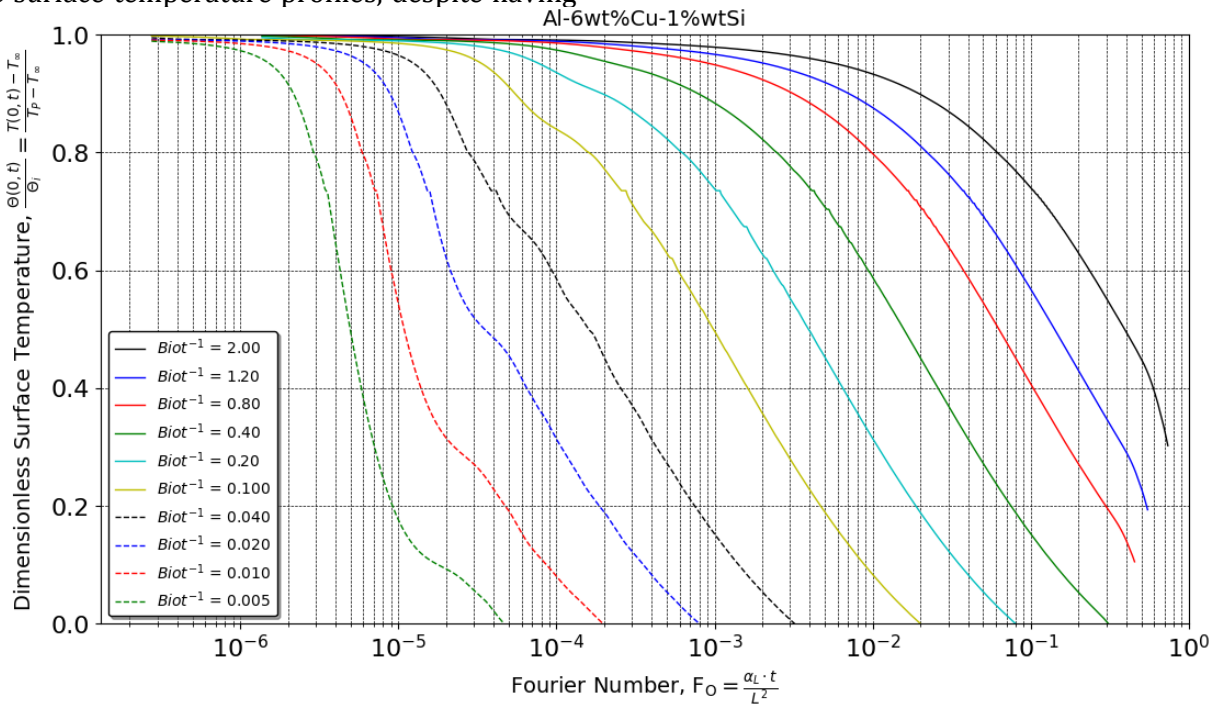

(a)

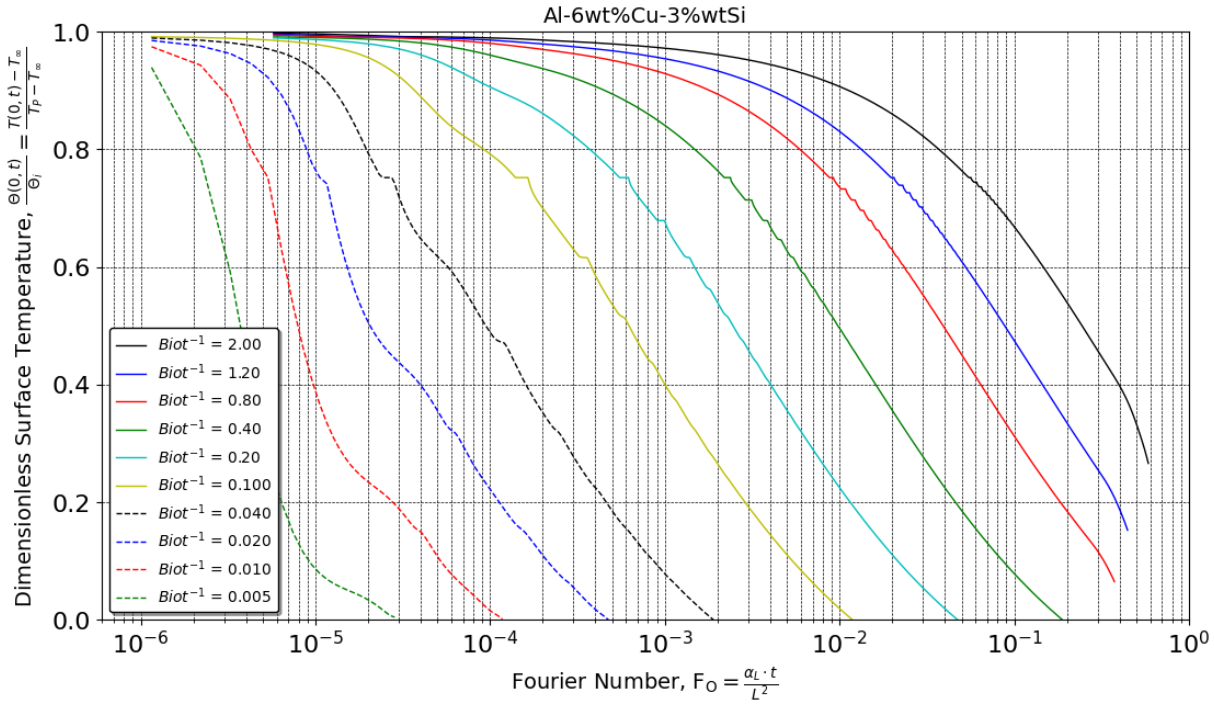

(b)

Fig. 4. Surface dimensionless temperature against Fourier number as a function of $Biot^{-1}$, (A) Al-6wt%Cu-1wt%Si and, (B) Al-6wt%Cu-3wt%Si alloy.

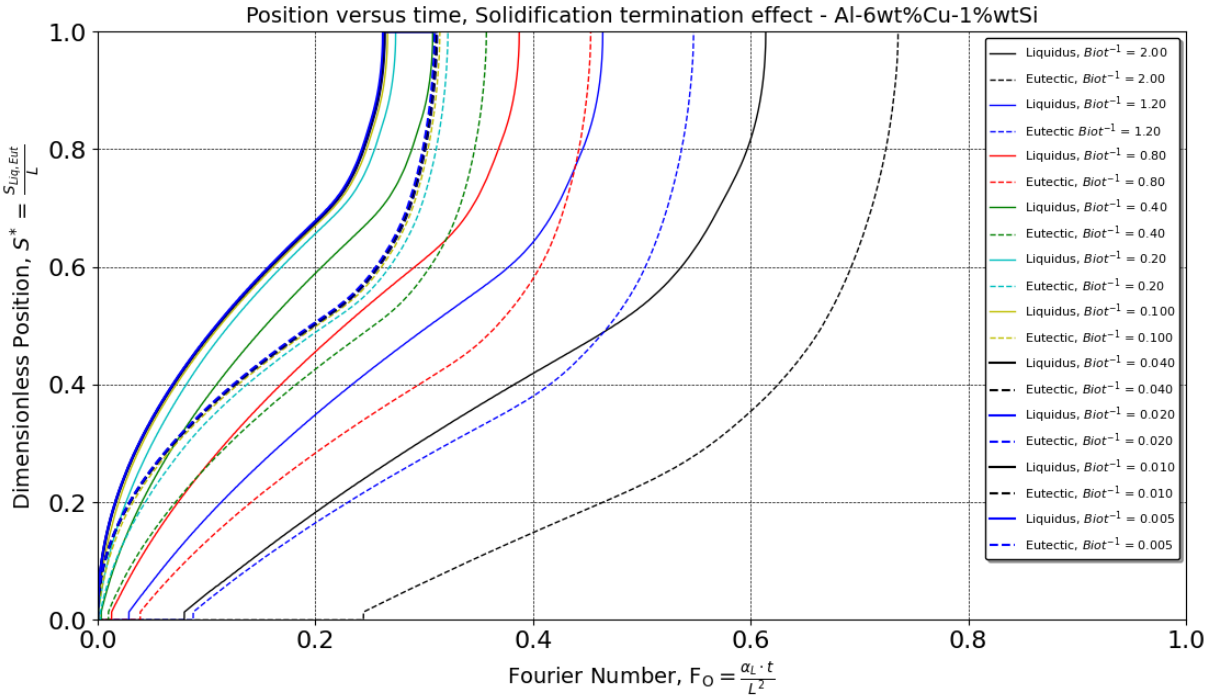

(a)

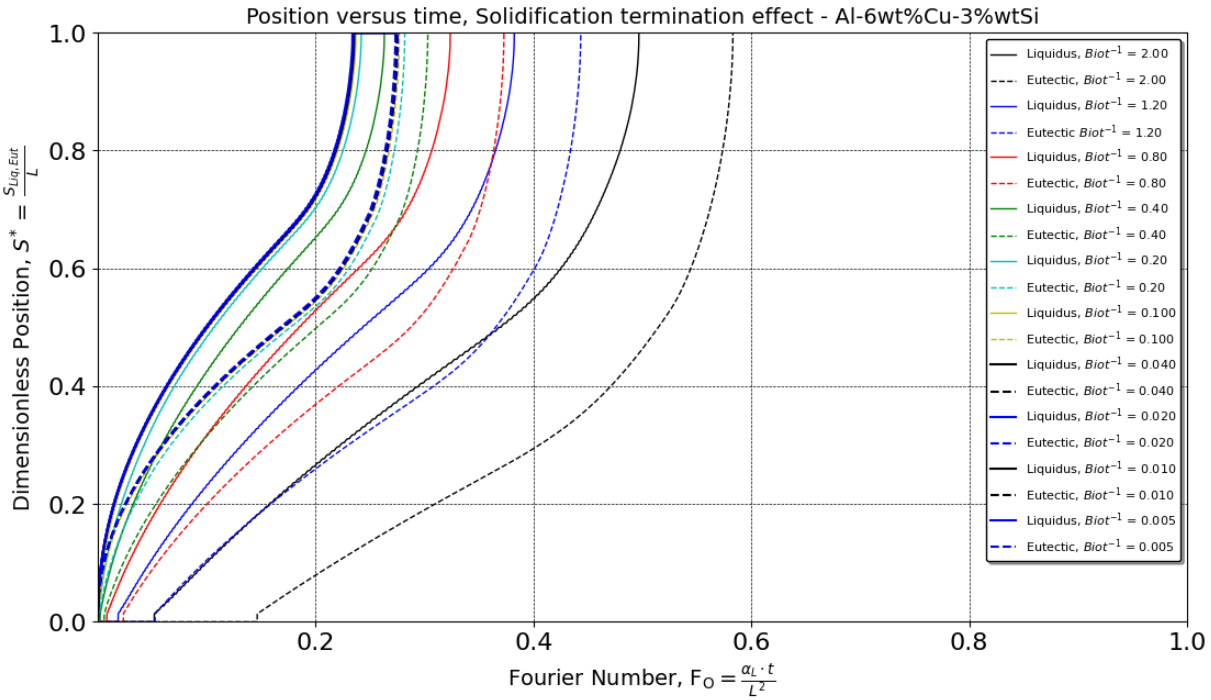

(b)

Fig. 5. Dimensionless position of liquidus and eutectic isotherms as a function of Fourier number for several $Biot^{-1}$ curves, (A) Al-6wt%Cu-1wt%Si and, (B) Al-6wt%Cu-3wt%Si alloy.

The dimensionless positions of liquidus and eutectic isotherms are expressed in terms of Fourier number of liquid phase $F_0 = \frac{\alpha_L t}{L^2}$ as shown in Fig. 5. By comparing Fig. 5A and Fig. 5B, it can be seen that the liquidus and eutectic isotherms of Al-6Cu-3Si (in wt %) alloy are more accelerated for a given Biot number. The change in isotherm positions of studied alloys implies in opposition to the non-reacting heat conduction. Therefore, Fourier number alone is not suitable to express the dimensionless time scale for the solidification of alloys, however, a certain combination of parameters considering Stefan number must be carried out to reduce

the items A and B of the Fig. 4 and Fig. 5 to singular curves for both regarded alloys. Furthermore, when Biot increases as a consequence the solidification time decreases from very distinct curves at low Biot numbers to similar curves at the beginning of solidification for high Biots, condition normally verified in rapid solidification like in laser surface treatment, whose thermal gradients are of $\sim 10^5$ K m^{-1} to 10^6 K m^{-1} due to a faster increasing thermal gradient at the eutectic interface, as recently demonstrated analytically for binary alloys [8].

Table 1. Thermophysical and transformation properties.

Properties	Symbol	Units	Al-6 wt. %Cu-1 wt. %Si	Al-6 wt. %Cu-3 wt. %Si
Liquidus temperature	T_L	$°C$	638	624.65
Solidus temperature	T_{EUT}	$°C$	530.2	525.07
	T_{SI}	$°C$	527.6	549.34
Liquidus slope	m_L^{Cu}	$°C(wt\%Cu)$	3.437	3.700
	m_L^{Si}	$°C(wt\%Si)$	7.091	7.422
Equilibrium partition coefficient	k_{Cu}		0.1028	0.1419
	k_{Si}		0.1120	0.1612
Activation energy (Al liquid)	${Q_d^{Cu}}_L$	$kJ\ mol^{-1}$	24	24
	${Q_d^{Si}}_L$	$kJ\ mol^{-1}$	30	30
Diffusion constant (Al liquid)	${D_0^{Cu}}_L$	$m^2\ s^{-1}$	3.0×10^{-9}	3.0×10^{-9}
	${D_0^{Si}}_L$	$m^2\ s^{-1}$	1.0×10^{-9}	1.0×10^{-9}
Activation energy (Al FCC)	Q_d^{Cu}	$kJ\ mol^{-1}$	130.2	130.2
	Q_d^{Si}	$kJ\ mol^{-1}$	137.0	137.0
Diffusion constant (Al FCC)	D_0^{Cu}	$m^2\ s^{-1}$	2.9 x 10^{-5}	2.9 x 10^{-5}
	D_0^{Si}	$m^2\ s^{-1}$	2.48 x 10^{-4}	2.48 x 10^{-4}
Thermal conductivity (solid)	k_S	$W\ m^{-1}K^{-1}$	180	161.0
Thermal conductivity (liquid)	k_L	$W\ m^{-1}K^{-1}$	87.9	66.9
Density (solid)	ρ_S	$kg\ m^{-3}$	2713.4	2733.4
Density (liquid)	ρ_L	$kg\ m^{-3}$	2529.5	2542.1
Specific heat (solid)	c_S	$J\ kg^{-1}K^{-1}$	1063	1099.0
Specific heat (liquid)	c_L	$J\ kg^{-1}K^{-1}$	1125	1116.0
Latent heat of fusion (FCC_A1)	ΔH_{FCC_A1}	$J\ kg^{-1}$	289600	260300
Latent heat of fusion ($SILICON$)	ΔH_{Si}		15800	50000
Latent heat of fusion ($EUTECTIC$)	ΔH_{Eut}		57200	72700
Dynamic viscosity of the liquid	μ_L	$kg\ m^{-1}s^{-1}$	3.0×10^{-3}	3.0×10^{-3}
Coefficient of thermal expansion	β_T	K^{-1}	-4.95×10^{-5}	-4.95×10^{-5}
Solutal expansion coefficient	β_c	$(\%)^{-1}$	-0.72	-0.72
Permeability constant	K_0	m^2	6.67×10^{-11}	6.67×10^{-11}

4. CONCLUSIONS

From the results obtained and discussed above, the following conclusions are deduced:

A wide range of $Biot$ number is analysed for the transient upward solidification of Al-6Cu-1Si and Al-6Cu-3Si (all in wt %) alloys for a magnitude of 10^6s time scale. By considering surface temperature as well as position of both liquidus and eutectic isotherms in relation to the Fourier number of the liquid phase, despite the similar behaviour of the solidification thermal variables, $\frac{\theta(0,t)}{\theta_i}$ and S^*, the difference in the solidification range, latent heat and other thermophysical properties provide distinct curves. The solidification local time is also affected by the kinetics. The maximum value applied to $Biot$ number in this study is 200. In this case, it can be observed that liquidus and eutectic curves are very close to each other, similarly to that verified for rapid solidification processes, where only a single solid/liquid interface is present due to the high thermal gradient at the eutectic interface be much greater than that at the liquidus isotherm,

as recently analytically demonstrated for binary alloys [8]. To get the same shape for the solidification variables for several compositions, a new parameter that comprised Ste number must be proposed for the case of dual moving boundary interfaces during alloys solidification.

A novel scheme is proposed for determining the solute redistribution coefficient β_i based on the SDAS Fourier number α_i calculated from the nucleation formulation recently derived by Ferreira et al. [34].

The nucleation/growth radius r is used to demonstrate a novel proposal in which the local Fourier number α_i is theoretically determined from a first- or second-order formulation nucleation model in terms of the thermal field tensor Γ.

This work may contribute to the understanding of how to manage solidification operational parameters aiming at designing of the LHTES reservoirs.

Acknowledgement

The authors acknowledge the financial support provided by CAPES (Coordenação de Aperfeiçoamento de Pessoal de Nível Superior - Brazil) Finance Code 001 and Grant 88881.707312/2022-01, and CNPq (National Council for Scientific and Technological Development - Brazil).

REFERENCES

[1] A. Garcia, T. W. Clyne, and M. Prates, "Mathematical model for the unidirectional solidification of metals: II. Massive molds," *Metallurgical Transactions B*, vol. 10, no. 1, pp. 85–92, Mar. 1979, doi: 10.1007/BF02653977.

[2] J. Crank, *Free and Moving Boundary Problems*. New York: Clarendon Press, 1987.

[3] Mohamed Zerroukat and Chris Chatwin, *Computational moving boundary problems*. New York: John Wiley & Sons Inc., 1994.

[4] J. Ni and C. Beckermann, "A volume-averaged two-phase model for transport phenomena during solidification," *Metallurgical Transactions B*, vol. 22, no. 3, pp. 349–361, Jun. 1991, doi: 10.1007/BF02651234.

[5] C. R. Swaminathan and V. R. Voller, "Towards a general numerical scheme for solidification systems," *Int J Heat Mass Transf*, vol. 40, no. 12, pp. 2859–2868, Aug. 1997, doi: 10.1016/S0017-9310(96)00329-8.

[6] V. R. Voller, "A similarity solution for the solidification of a multicomponent alloy," *Int J Heat Mass Transf*, vol. 40, no. 12, pp. 2869–2877, Aug. 1997, doi: 10.1016/S0017-9310(96)00330-4.

[7] V. R. Voller and S. Roscani, "A general non-Fourier Stefan problem formulation that accounts for memory effects," *Int J Heat Mass Transf*, vol. 209, p. 124094, Aug. 2023, doi: 10.1016/j.ijheatmasstransfer.2023.124094.

[8] I. L. Ferreira, A. Garcia, and A. L. S. Moreira, "On the Multiscale Formulation and the Derivation of Phase-Change Moving Interfaces," *Int J Thermophys*, vol. 44, no. 1, p. 2, Jan. 2023, doi: 10.1007/s10765-022-03099-6.

[9] L. Yang, X. Jin, Y. Zhang, and K. Du, "Recent development on heat transfer and various applications of phase-change materials," *J Clean Prod*, vol. 287, p. 124432, Mar. 2021, doi: 10.1016/j.jclepro.2020.124432.

[10] A. Sharma, V. V. Tyagi, C. R. Chen, and D. Buddhi, "Review on thermal energy storage with phase change materials and applications," *Renewable and Sustainable Energy Reviews*, vol. 13, no. 2, pp. 318–345, Feb. 2009, doi: 10.1016/j.rser.2007.10.005.

[11] N.-K. Kim, M.-H. Shim, and D. Won, "Building Energy Management Strategy Using an HVAC System and Energy Storage System," *Energies (Basel)*, vol. 11, no. 10, p. 2690, Oct. 2018, doi: 10.3390/en11102690.

[12] M. Iten, S. Liu, and A. Shukla, "A review on the air-PCM-TES application for free cooling and heating in the buildings," *Renewable and Sustainable Energy Reviews*, vol. 61, pp. 175–186, Aug. 2016, doi: 10.1016/j.rser.2016.03.007.

[13] Z. Qiu and L. Li, "Experimental and numerical investigation of laminar heat transfer of microencapsulated phase change material slurry (MPCMS) in a circular tube with constant heat flux," *Sustain Cities Soc*, vol. 52, p. 101786, Jan. 2020, doi: 10.1016/j.scs.2019.101786.

[14] C. Zhou and S. Wu, "Medium- and high-temperature latent heat thermal energy storage: Material database, system review, and corrosivity assessment," *Int J Energy Res*, vol. 43, no. 2, pp. 621–661, Feb. 2019, doi: 10.1002/er.4216.

[15] A. Pasupathy, R. Velraj, and R. V. Seeniraj, "Phase change material-based building architecture for thermal management in residential and commercial establishments," *Renewable and Sustainable Energy Reviews*, vol. 12, no. 1, pp. 39–64, Jan. 2008, doi: 10.1016/j.rser.2006.05.010.

[16] Z.-A. Liu *et al.*, "Effectiveness assessment of different kinds/configurations of phase-change materials (PCM) for improving the thermal performance of lightweight building walls in summer and winter," *Renew Energy*, vol. 202, pp. 721–735, Jan. 2023, doi: 10.1016/j.renene.2022.12.009.

[17] D. Govindasamy and A. Kumar, "Experimental analysis of solar panel efficiency improvement with composite phase change materials," *Renew Energy*, vol. 212, pp. 175–184, Aug. 2023, doi: 10.1016/j.renene.2023.05.028.

[18] J.-X. Wang *et al.*, "A scalable micro-encapsulated phase change material and liquid metal integrated composite for sustainable data center cooling," *Renew Energy*, vol. 213, pp. 75–85, Sep. 2023, doi: 10.1016/j.renene.2023.05.106.

[19] Y. Maleki, F. Pourfayaz, and M. Mehrpooya, "Experimental study of a novel hybrid photovoltaic/thermal and thermoelectric generators system with dual phase change materials," *Renew Energy*, vol. 201, pp. 202–215, Dec. 2022, doi: 10.1016/j.renene.2022.11.037.

[20] B. Ryu *et al.*, "Best thermoelectric efficiency of ever-explored materials," *iScience*, vol. 26, no. 4, p. 106494, Apr. 2023, doi: 10.1016/j.isci.2023.106494.

[21] M. Muñoz, A. Rovira, and M. J. Montes, "Thermodynamic cycles for solar thermal power plants: A review," *WIREs Energy and Environment*, vol. 11, no. 2, Mar. 2022, doi: 10.1002/wene.420.

[22] K. Ikhlef, S. Larbi, and İ. Üçgül, "Experimental study of different thermal storage system effects on the performance of a small prototype solar chimney power plant," *Renew Energy*, vol. 200, pp. 516–526, Nov. 2022, doi: 10.1016/j.renene.2022.09.087.

[23] H. Bouziane and B. Benhamou, "Assessment of the impact of thermal energy storage operation strategy on parabolic trough solar power plant performance," *Renew Energy*, vol. 202, pp. 713–720, Jan. 2023, doi: 10.1016/j.renene.2022.11.119.

[24] I. L. Ferreira, C. A. Santos, A. Garcia, and V. R. Voller, "Analytical, numerical, and experimental analysis of inverse macrosegregation during upward unidirectional solidification of Al-Cu alloys," *Metallurgical and Materials Transactions B*, vol. 35, no. 2, pp. 285–297, Apr. 2004, doi: 10.1007/s11663-004-0030-8.

[25] I. L. Ferreira, V. R. Voller, B. Nestler, and A. Garcia, "Two-dimensional numerical model for the analysis of macrosegregation during solidification," *Comput Mater Sci*, vol. 46, no. 2, pp. 358–366, Aug. 2009, doi: 10.1016/j.commatsci.2009.03.020.

[26] A. P. Boeira, I. L. Ferreira, and A. Garcia, "Modeling of macrosegregation and microporosity formation during transient directional solidification of aluminum alloys," *Materials Science and Engineering: A*, vol. 435–436, pp. 150–157, Nov. 2006, doi: 10.1016/j.msea.2006.06.003.

[27] A. P. Boeira, I. L. Ferreira, and A. Garcia, "Alloy composition and metal/mold heat transfer efficiency affecting inverse segregation and porosity of as-cast Al–Cu alloys," *Mater Des*, vol. 30, no. 6, pp. 2090–2098, Jun. 2009, doi: 10.1016/j.matdes.2008.08.032.

[28] F. C. Nascimento, M. C. C. Paresque, J. A. de Castro, P. A. D. Jácome, A. Garcia, and I. L. Ferreira, "Application of computational thermodynamics to the determination of thermophysical properties as a function of temperature for multicomponent Al-based alloys," *Thermochim Acta*, vol. 619, pp. 1–7, Nov. 2015, doi: 10.1016/j.tca.2015.09.013.

[29] V. R. Voller, "On a general back-diffusion parameter," *J Cryst Growth*, vol. 226, no. 4, pp. 562–568, Aug. 2001, doi: 10.1016/S0022-0248(01)01411-7.

[30] I. L. Ferreira *et al.*, "On an expression for the growth of secondary dendrite arm spacing during non-equilibrium solidification of multicomponent alloys: Validation against ternary aluminum-based alloys," *J Manuf Process*, vol. 35, pp. 634–650, Oct. 2018, doi: 10.1016/j.jmapro.2018.08.010.

[31] T. W. Clyne and W. Kurz, "Solute redistribution during solidification with rapid solid-state diffusion," *Metallurgical Transactions A*, vol. 12, no. 6, pp. 965–971, Jun. 1981, doi: 10.1007/BF02643477.

[32] M. Rappaz and W. J. Boettinger, "On dendritic solidification of multicomponent alloys with unequal liquid diffusion coefficients," *Acta Mater*, vol. 47, no. 11, pp. 3205–3219, Sep. 1999, doi: 10.1016/S1359-6454(99)00188-3.

[33] W. Kurz, M. Rappaz, and R. Trivedi, "Progress in modelling solidification microstructures in metals and alloys. Part II: dendrites from 2001 to 2018," *International Materials Reviews*, vol. 66, no. 1, pp. 30–76, Jan. 2021, doi: 10.1080/09506608.2020.1757894.

[34] I. L. Ferreira and A. L. S. Moreira, "On the Continuous Mechanics First and Second-Order Formulations for Nonequilibrium Nucleation: Derivation and Applications," *Int J Thermophys*, vol. 44, no. 5, p. 72, May 2023, doi: 10.1007/s10765-023-03178-2.

[35] A. L. London and R. A. Seban, "Rate of ice formation," *Transactions of the ASME*, vol. 65, pp. 771–778, 1943.